



Publication Year	2015
Acceptance in OA @INAF	2020-03-05T15:52:46Z
Title	Interstellar Dust Charging in Dense Molecular Clouds: Cosmic Ray Effects
Authors	Ivlev, A. V.; Padovani, Marco; GALLI, Daniele; Caselli, P.
DOI	10.1088/0004-637X/812/2/135
Handle	http://hdl.handle.net/20.500.12386/23139
Journal	THE ASTROPHYSICAL JOURNAL
Number	812

INTERSTELLAR DUST CHARGING IN DENSE MOLECULAR CLOUDS: COSMIC RAY EFFECTS

A. V. IVLEV¹, M. PADOVANI^{2,3}, D. GALLI³, AND P. CASELLI¹

¹Max-Planck-Institut für Extraterrestrische Physik, D-85741 Garching, Germany; ivlev@mpe.mpg.de

²Laboratoire Univers et Particules de Montpellier, UMR 5299 du CNRS, Université de Montpellier, F-34095 Montpellier, France

³INAF-Osservatorio Astrofisico di Arcetri, I-50125 Firenze, Italy

Received 2015 June 17; accepted 2015 August 30; published 2015 October 16

ABSTRACT

The local cosmic-ray (CR) spectra are calculated for typical characteristic regions of a cold, dense molecular cloud to investigate two mechanisms of dust charging that have, thus far, been neglected: the collection of suprathermal CR electrons and protons by grains and photoelectric emission from grains due to the UV radiation generated by CRs. These two mechanisms add to the conventional charging by ambient plasma, produced in the cloud by CRs. We show that the CR-induced photoemission can dramatically modify the charge distribution function for submicron grains. We demonstrate the importance of the obtained results for dust coagulation: while the charging by ambient plasma alone leads to a strong Coulomb repulsion between grains and inhibits their further coagulation, the combination with the photoemission provides optimum conditions for the growth of large dust aggregates in a certain region of the cloud, corresponding to the densities $n(\text{H}_2)$ between $\sim 10^4$ and $\sim 10^6 \text{ cm}^{-3}$. The charging effect of CRs is of a generic nature, and is therefore expected to operate not only in dense molecular clouds but also in the upper layers and the outer parts of protoplanetary disks.

Key words: cosmic rays – dust, extinction – ISM: clouds

1. INTRODUCTION

Interstellar dust grains in dense molecular clouds are subject to several electric charging processes (e.g., Draine & Salpeter 1979; Draine & Sutin 1987; Weingartner & Draine 2001b). The resulting net electric charge carried by micron or sub-micron-size grains has important consequences for the chemical and dynamical evolution of molecular clouds: it affects the process of dust coagulation (Dominik et al. 2007; Okuzumi 2009), the rate of grain-catalyzed electron-ion recombination (Mestel & Spitzer 1956; Watson 1974), the amount of gas-phase elemental depletion (Spitzer 1941), and the electrical resistivity of the cloud’s plasma (Elmegreen 1979; Wardle & Ng 1999). The resistivity, in turn, controls the coupling between the neutral gas and the interstellar magnetic field, and eventually the dynamics of gravitational collapse of molecular clouds and the formation of stars (e.g., Nakano et al. 2002; Shu et al. 2006).

Collisions of dust grains with the plasma of thermal electrons and ions from the gas (hereafter, cold plasma charging) represent an important dust charging process in molecular clouds (e.g., Draine & Sutin 1987; Draine 2011). Since electrons of mass m_e have a thermal speed that is much larger than that of ions of mass m_i (by a factor of $\sqrt{m_i/m_e} \gg 1$), by this process, grains acquire a (predominantly) negative charge. The photoelectric effect (also called photoemission), on the other hand, results in the positive charging of dust grains, and is set by the radiation field in the cloud at energies above a few electronvolts. Photoemission is an important charging process for diffuse gas with visual extinction $A_V \lesssim 10$ (e.g., Bakes & Tielens 1994; Weingartner & Draine 2001b). As the interstellar radiation field is exponentially attenuated with increasing A_V , photoemission is usually neglected to compute the charge distribution of grains in the dense gas of molecular cloud cores (e.g., Umebayashi & Nakano 1980; Nishi et al. 1991).

Cold plasma charging and photoemission are usually assumed to be the dominant grain charging mechanisms in

the cold interstellar medium. In this paper, we study the effects of cosmic rays (CRs) on the charging of submicron dust grains in molecular clouds. We focus on two charging processes that contribute in addition to the cold-plasma charging, but have been neglected so far. By calculating the local CR spectra for typical cloud regions, we investigate the effects of (1) the collection of suprathermal CR electrons and protons by grains (Shchekinov 2007) and (2) the photoelectric emission from grains due to the UV radiation generated by CRs. Using the cold-plasma collection as the “reference case,” we show that the photoelectric emission can dramatically modify the charge distribution function for dust in almost the entire cloud and discuss important implications of the obtained results. In particular, we point out that while the cold-plasma charging alone leads to a strong Coulomb repulsion between grains and inhibits their further coagulation, the combination with the CR-induced photoemission provides optimum conditions for the growth of large dust aggregates in a certain region of the cloud.

2. CR PROPERTIES RELEVANT TO DUST CHARGING

The specific intensities (or spectra) of CR protons and electrons inside a dense molecular cloud are determined by the interstellar CR spectra. In order to constrain the trend of the interstellar spectra at high energies ($E \gtrsim 500 \text{ MeV}$), we use the latest results of the Alpha Magnetic Spectrometer (AMS-02), mounted on the International Space Station (Aguilar et al. 2014, 2015). The high-energy spectrum slope is -3.2 for electrons, while for protons it is -2.7 .

At lower energies, the shape of the interstellar CR spectrum is highly uncertain due to the effect of solar modulation (see, e.g., Putze et al. 2011). Data collected by the *Voyager 1* spacecraft from a region beyond the solar termination shock are extremely useful in this context (Webber 1998) because they provide a lower limit to the CR spectrum in the energy range from ~ 5 to $\sim 50 \text{ MeV}$ that should not be too different from the actual interstellar value (Stone et al. 2013).

However, two caveats should be kept in mind. First, *Voyager 1* has not yet entered interstellar space because the magnetic field detected by magnetometers on board the spacecraft still retains some characteristics of the solar wind magnetic field (Burlaga & Ness 2014). Therefore, the measured proton fluxes may still contain a fraction of anomalous CRs from inside the heliosphere (Scherer et al. 2008). Second, even if *Voyager 1* were in the interstellar space, there is no guarantee that the measured spectra of CR protons and electrons are representative of the *average* Galactic spectra because the contribution of local sources (i.e., within parsecs from the Sun) is difficult to quantify. Nevertheless, the *Voyager 1* data provide the only *direct* observational constraint presently available on the low-energy spectra of CRs, and therefore they cannot be discarded. In particular, we use the results of Stone et al. (2013), obtained from data collected by *Voyager 1* since 2012 August, when the spacecraft was at a heliocentric distance of 122 AU.

We model the low-energy behavior of the proton and electron spectra with power-law dependencies. To describe a crossover to the high-energy scalings, we employ the simple analytical expression

$$j_k(E) = C \frac{E^\alpha}{(E + E_0)^\beta} \text{eV}^{-1} \text{cm}^{-2} \text{s}^{-1} \text{sr}^{-1}, \quad (1)$$

where $k = p, e$ and the crossover energy $E_0 = 500 \text{ MeV}$ is the same for both species. Following Stone et al. (2013), for CR electrons we adopt a low-energy spectrum slope of $\alpha = -1.5$, while for protons we explore two extreme cases with $\alpha = -0.8$ and $\alpha = 0.1$. The resulting interstellar spectra are presented in Figure 1, other parameters for Equation (1) are listed in Table 1. Combinations of the two proton spectra with the electron spectrum are termed below as the model \mathcal{H} (“High,” $\alpha = -0.8$) and model \mathcal{L} (“Low,” $\alpha = 0.1$).

The number densities for the CR species are given by $n_{\text{CR},k} = 4\pi \int_{E_{\text{cut}}}^{\infty} dE j_k(E) / v_k(E)$, where $v_k(E)$ is the velocity for the energy E . In order to preserve charge neutrality of CRs, we set $n_{\text{CR},p} = n_{\text{CR},e}$, which yields the lower energy cutoff $E_{\text{cut}} \simeq 5 \text{ keV}$ and $\simeq 2 \text{ MeV}$ for the models \mathcal{H} and \mathcal{L} , respectively. The corresponding energy densities are defined by $\varepsilon_{\text{CR},k} = 4\pi \int_{E_{\text{cut}}}^{\infty} dE E j_k(E) / v_k(E)$. The total energy density, $\varepsilon_{\text{CR},p} + \varepsilon_{\text{CR},e}$, is dominated by protons and varies between $\simeq 0.78 \text{ eV cm}^{-3}$ (model \mathcal{L}) and $\simeq 1.54 \text{ eV cm}^{-3}$ (model \mathcal{H}).

We note that our choice of a single interstellar spectrum for CR electrons and two possible spectra for CR protons is arbitrary. As discussed above, we adopt the view that the *Voyager 1* data represent lower limits to the actual spectra, due to residual modulation of the interstellar fluxes at the current position of the spacecraft. For simplicity, this remaining uncertainty is attributed to the protons only: we select the “minimum” proton spectrum ($\alpha = 0.1$) compatible with the data, and the “maximum” spectrum ($\alpha = -0.8$) providing the upper bound for the available observational data on the CR ionization rate (see Section 2.1).

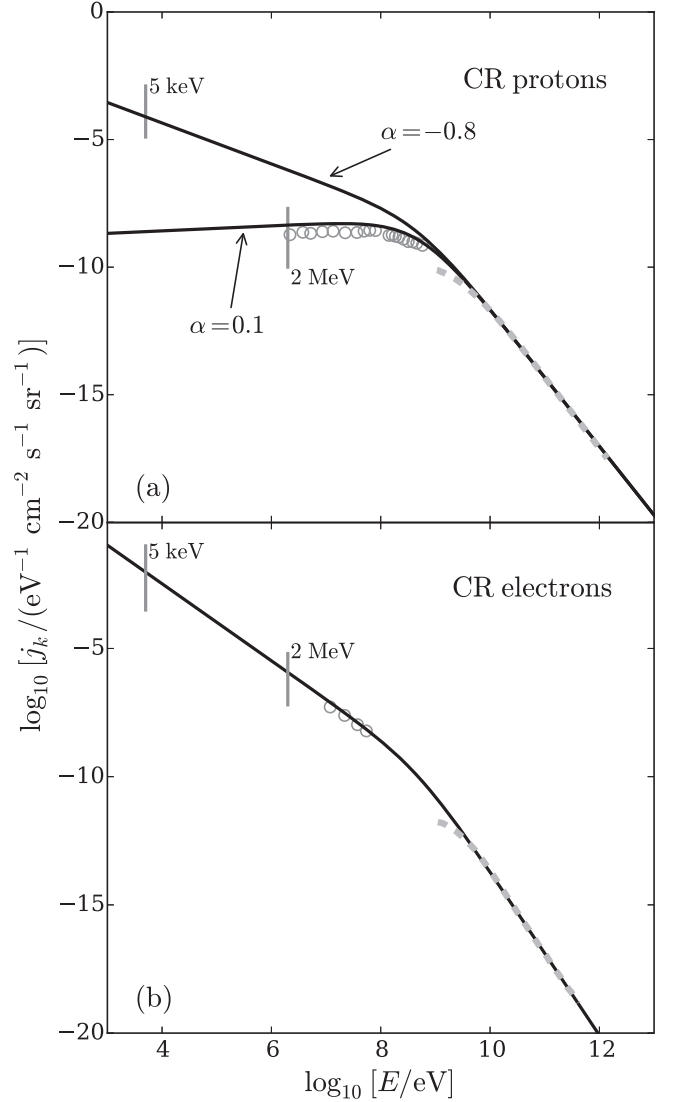


Figure 1. Interstellar spectra of CR protons (a) and electrons (b). The black solid lines show the parameterized spectra given by Equation (1), open circles represent the *Voyager 1* data (Stone et al. 2013), and gray dashed lines are the AMS-02 data (Aguilar et al. 2014, 2015). A combination of the given electron spectrum with the proton spectrum for $\alpha = -0.8$ and $\alpha = 0.1$ is referred to as the CR model \mathcal{H} and \mathcal{L} , respectively. The respective lower energy cutoff E_{cut} ($\simeq 5 \text{ keV}$ and $\simeq 2 \text{ MeV}$) is indicated by the gray vertical bars.

Table 1
Parameters of Interstellar CR Spectra, Equation (1)

Species (k)	C	α	β	$\beta - \alpha$
Electrons	2.1×10^{18}	-1.5	1.7	3.2
Protons (model \mathcal{H})	2.4×10^{15}	-0.8	1.9	2.7
Protons (model \mathcal{L})	2.4×10^{15}	0.1	2.8	2.7

2.1. Local CR Spectra

In order to concentrate on the charging effects induced by CRs, we adopt an idealized 1D (slab) model of a dense core embedded in a molecular cloud (for details, see Padovani et al. 2009). We assume that CRs propagate normally to the

surface in straight lines, with half of the interstellar CR flux incident on each side of the cloud.⁴ This simple model, neglecting integration over the incidence angles, yields the local spectra that approach the exact results in the inner core region, while in the outer region the fluxes are only slightly overestimated (by less than 30%; details will be presented elsewhere).

For the core, we use the density profile of a Bonnor–Ebert sphere (Ebert 1955; Bonnor 1956), which typically well reproduces observations of starless cores (e.g., Alves et al. 2001; Keto & Caselli 2008; André et al. 2014). In particular, we consider a centrally concentrated core, such as L1544, where the volume density within the central 500 AU is $n(\text{H}_2) = 2 \times 10^7 \text{ cm}^{-3}$, one of the largest known for starless cores (Keto & Caselli 2010). The molecular core has a radius of about 0.1 pc, beyond which the density drops below $n(\text{H}_2) = 10^4 \text{ cm}^{-3}$ and photoprocesses becomes important (Keto & Caselli 2010). We further assume that the core is embedded in an envelope of lower density, to simulate the location of the dense core in a molecular cloud such as Taurus. Such an envelope extends up to a distance of 4.4 pc from the core center, and the average density within a radius of 4.4 pc is 230 cm^{-3} . With these properties, the cloud has a mass column density of $144 M_\odot \text{ pc}^{-2}$, which is typical of molecular clouds (Roman-Duval et al. 2010).

To demonstrate the extent to which the dust charges in dense molecular clouds are expected to be affected by CRs, we consider three characteristic regions of the embedded core: the outer boundary [$n(\text{H}_2) = 10^4 \text{ cm}^{-3}$, $N(\text{H}_2) = 3.2 \times 10^{21} \text{ cm}^{-2}$], the inner core [$n(\text{H}_2) = 10^6 \text{ cm}^{-3}$, $N(\text{H}_2) = 2.8 \times 10^{22} \text{ cm}^{-2}$], and also the core center [$n(\text{H}_2) = 2 \times 10^7 \text{ cm}^{-3}$, $N(\text{H}_2) = 10^{23} \text{ cm}^{-2}$]. We shall refer to these regions as “outer” (O), “inner” (I), and “center” (C), respectively.

The CR protons and electrons penetrating the cloud ionize the neutral gas, i.e., produce a local plasma environment whose properties are determined by the value of $N(\text{H}_2)$. On the other hand, the ionization yields a major contribution to the energy loss of CRs (see Appendix A), thus modifying the interstellar spectra to the local form (Padovani et al. 2009). The low-energy CR species as well as the multiple generations of electrons and ions formed in the ionization avalanche (see Appendix B) rapidly lose their energy: the characteristic energy loss timescale τ_{stop} , given by Equation (15), is always much shorter than the timescale of recombination. Therefore, the steady-state energy distribution of electrons and ions in a dense cloud can be viewed as a superposition of two distinct parts: a cold Maxwellian peak where electrons and ions accumulate and eventually recombine—that dominates the total plasma density, and a suprathermal tail representing the modified (propagated) CR spectrum—that determines the ionization rate.

The local steady-state equilibrium is determined by the balance between the CR ionization of H_2 and various recombination processes (see, e.g., Oppenheimer & Dalgarno 1974; McKee 1989). A competition between the dissociative recombination with molecular ions and the radiative recombination with heavy metal ions (in the presence of charge-transfer reactions) occurring in different core regions

can significantly alter the magnitude of the electron fraction $x_e = n_e/n(\text{H}_2)$ and, in particular, modify the dependence on $n(\text{H}_2)$. For the L1544 core, we employ the following interpolation formula (Caselli et al. 2002, their model 3):

$$x_e \simeq 6.7 \times 10^{-6} \left(\frac{n(\text{H}_2)}{\text{cm}^{-3}} \right)^{-0.56} \sqrt{\frac{\zeta}{10^{-17} \text{ s}^{-1}}}, \quad (2)$$

where ζ is the CR ionization rate.⁵ In the following, we assume that the electron density n_e is equal to the density of all ion species formed in the ionization avalanche (i.e., the contribution of charged grains into the charge neutrality is negligible, see Section 3).

Figure 2 shows the combination of the propagated spectra and the cold Maxwellian background. The energy E_{int} at which the intersection between the two curves occurs is practically the same for all considered cases, $E_{\text{int}} \simeq 1.5 \times 10^{-2} \text{ eV}$.

Figure 3(a) shows the ionization rate as a function of the molecular H_2 column density for the two CR models. The characteristic values of ζ and the corresponding x_e are summarized in Table 2. For comparison, the values of ζ obtained by integrating the *Voyager 1* fluxes down to the lowest measured energy, without any extrapolation, are $\zeta = 1.2 \times 10^{-17} \text{ s}^{-1}$ and $\zeta = 2.8 \times 10^{-18} \text{ s}^{-1}$ for protons and electrons, respectively. These should be considered as lower limits to the interstellar value of ζ . Notice that the contribution of CR electrons to the average interstellar CR ionization rate, often neglected in the past, could be significant (although, in general, it is smaller than that of protons and heavier nuclei).

We point out that the main positive charge carrier changes across the cloud, because the molecular freeze-out becomes more efficient toward the core center (see, e.g., Tafalla et al. 2002). In this paper, we do not discuss a complex plasma chemistry, but instead consider two extreme cases when the dominant ions are either H^+ (for the strongly depleted inner dense regions) or HCO^+ (for the outer regions). In Section 3.3, we demonstrate that the plasma composition has only a minor effect on the obtained results.

2.2. Local Radiation Field

The local radiation is generated by CRs via the following three (prime) mechanisms: the CR electron Bremsstrahlung, the π^0 decay, and the H_2 fluorescence.

We calculate the bremsstrahlung spectrum following Blumenthal & Gould (1970). For all three characteristic core regions, the resulting photoemission flux from a grain is much smaller than the collection flux of the surrounding cold-plasma ions, which indicates that the CR bremsstrahlung cannot contribute to dust charging (see Section 3.2). For the photon spectrum due to π^0 decay, we follow Kamae et al. (2006). This yields the photoemission flux, which is even smaller than that due to bremsstrahlung and, hence, is negligible, too. Note that for energies larger than the pion production threshold (280 MeV), both our CR proton spectra coincide and remain unmodified up to $N(\text{H}_2) \sim 10^{23} \text{ cm}^{-2}$.

Finally, following Equation (21) in Cecchi-Pestellini & Aiello (1992), we compute the H_2 fluorescence generated by CRs in the Lyman and Werner bands. The resulting flux of UV photons F_{UV} (in the energy range between 11.2 and 13.6 eV)

⁴ More advanced models should take into account the fact that molecular clouds are magnetized and CRs gyrate along magnetic field lines in addition to being scattered by magnetic fluctuations on the scale of the particle gyroradius. For a detailed treatment of these effects, see Padovani & Galli (2011), Padovani et al. (2013, 2014), and Morlino & Gabici (2015).

⁵ We note that the results presented in Section 3 practically do not depend on the precise form of the formula for x_e .

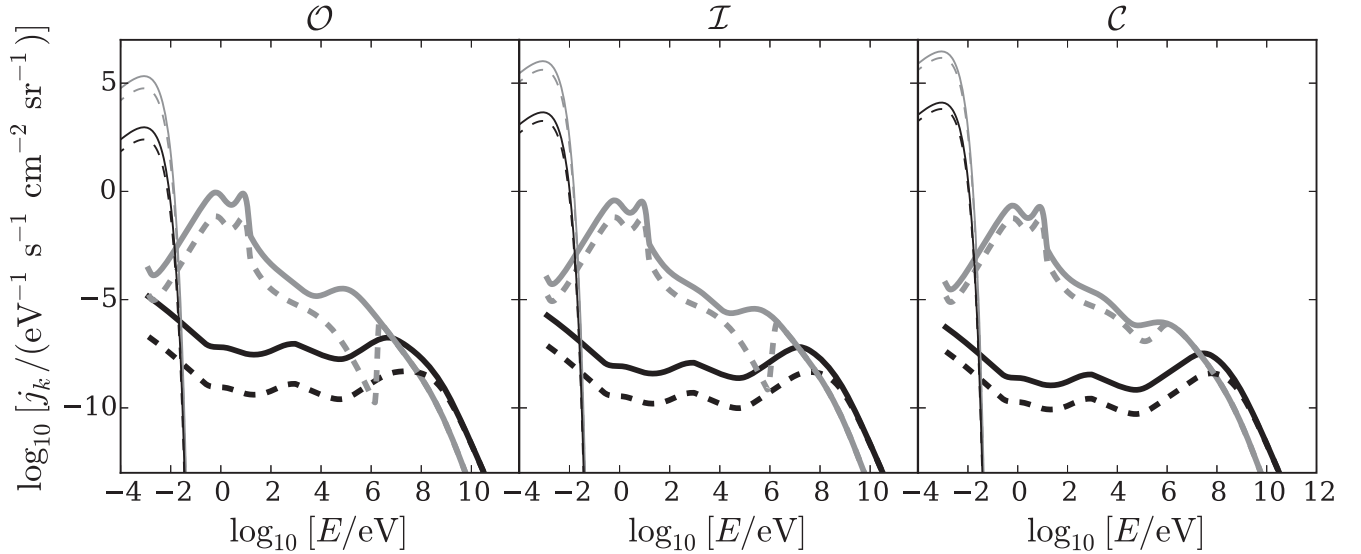


Figure 2. Local CR spectra for the model \mathcal{H} (solid lines) and model \mathcal{L} (dashed lines). The three panels show the results for the three typical characteristic regions of a dense core: “outer” (O), “inner” (I), and “center” (C). The thin lines represent a cold Maxwellian plasma background, and the thick lines are for the suprathermal propagated CR spectra. The gray and black lines correspond to electrons and protons, respectively. The presented results are for the case when H^+ are the dominant ions in a cold plasma; when heavier ions dominate, the Maxwellian spectra for ions should be divided by a square root of the corresponding atomic mass number.

can be approximately calculated assuming that the band excitation rates, being normalized by ζ , do not depend on the shape of the CR spectrum:⁶

$$F_{\text{UV}} \simeq 960 \left(\frac{1}{1 - \omega} \right) \left(\frac{\zeta}{10^{-17} \text{ s}^{-1}} \right) \times \left(\frac{N(\text{H}_2)/A_V}{10^{21} \text{ cm}^{-2} \text{ mag}^{-1}} \right) \left(\frac{R_V}{3.2} \right)^{1.5} \text{ cm}^{-2} \text{ s}^{-1}. \quad (3)$$

Here, ω is the dust albedo at ultraviolet wavelengths, and R_V is a measure of the slope of the extinction at visible wavelengths (e.g., Draine 2011). Assuming $\omega = 0.5$ and $R_V = 3.1$ (Cecchi-Pestellini & Aiello 1992)⁷ and substituting the typical gas-to-extinction ratio of $N(\text{H}_2)/A_V = 10^{21} \text{ cm}^{-2} \text{ mag}^{-1}$, we get $F_{\text{UV}} \simeq 1830(\zeta/10^{-17} \text{ s}^{-1})$. In Section 3, it is shown that the resulting photoelectric emission from dust grains can significantly exceed the cold-ion collection. Thus, the strongest radiation field generated by CRs is due to the H_2 fluorescence.

The interstellar radiation field is exponentially attenuated in the cloud. The specific intensity at the frequency ν decreases as $I(\nu) = I_{\text{IS}}(\nu)e^{-\tau_\nu}$, where $I_{\text{IS}}(\nu)$ is the intensity of the interstellar radiation field according to (Draine 2011) and $\tau_\nu = A_\nu/1.086$ is the optical depth. By integrating $I(\nu)/h\nu$ over $h\nu \geq 10 \text{ eV}$ (at lower frequencies, the photoelectric yield from dust grains rapidly falls off, so the radiation does not contribute to the photoemission), we derive the interstellar photon flux as a function of $N(\text{H}_2)$. The latter is plotted in Figure 3(b) and compared with F_{UV} versus $N(\text{H}_2)$ calculated for the models \mathcal{H} and \mathcal{L} . We see that the photon flux generated by CRs only slightly decreases

(model \mathcal{H}) or remains practically constant (model \mathcal{L}) in the shown range of $N(\text{H}_2)$; even for the maximum value of $R_V = 5.5$, the interstellar flux becomes negligible at $N(\text{H}_2) \gtrsim 3 \times 10^{21} \text{ cm}^{-2}$. We conclude that for all three core regions the radiation field is solely due to CRs.

3. CHARGE DISTRIBUTION FUNCTION OF DUST

The discrete charge distribution $N(Z) \equiv N_Z$ for dust grains of a given size a is normalized to the total differential dust density at that size, i.e., $\sum_Z N_Z = dn_d(a)/da$. The charge distribution is derived from the detailed equilibrium of the charging master equation (Draine & Sutin 1987),

$$J_e(Z+1)N_{Z+1} = \left[\sum_i J_i(Z) + J^{\text{PE}}(Z) \right] N_Z. \quad (4)$$

Here, $J_{e,i}(Z) = J_{e,i}^{\text{M}}(Z) + J_{e,i}^{\text{CR}}(Z)$ is the electron/ion collection flux, which has contributions from the cold Maxwellian plasma background (first term) and from the suprathermal low-energy part of the CR spectra (second term), and $J^{\text{PE}}(Z)$ is the photoemission flux due to the local radiation field.

We introduce the floating potential $\varphi_Z = Ze^2/a$ of a particle with the charge Ze . The collection fluxes of cold electrons and ions are obtained from the so-called “orbital motion limited” (OML) approximation (Whipple 1981; Fortov et al. 2005):

$$J_e^{\text{M}}(Z) = 2\sqrt{2\pi} a^2 n_e v_e \begin{cases} e^{\varphi_Z/k_B T}, & Z \leq 0; \\ (1 + \varphi_Z/k_B T), & Z \geq 0, \end{cases} \quad (5)$$

and

$$J_i^{\text{M}}(Z) = 2\sqrt{2\pi} a^2 n_i v_i \begin{cases} (1 - \varphi_Z/k_B T), & Z \leq 0; \\ e^{-\varphi_Z/k_B T}, & Z \geq 0, \end{cases} \quad (6)$$

where $v_{e,i} = \sqrt{k_B T/m_{e,i}}$ are the thermal velocity scales. Note that for the sake of clarity the (minor) effect of the polarization interaction, omitted in these equations, is discussed later.

⁶ In fact, the excitation and ionization cross sections have somewhat different dependencies on energy. For this reason, the normalized excitation rate by CR electrons, obtained with the spectra shown in Figure 2, is about 2.2–2.8 times larger than that reported in Cecchi-Pestellini & Aiello (1992). However, we were not able to find a reliable expression for the excitation cross section by protons, and therefore employ the approximate Equation (3).

⁷ According to Gordon (2004), in dense cores with $R_V \gtrsim 5$ the dust albedo may be closer to 0.3.

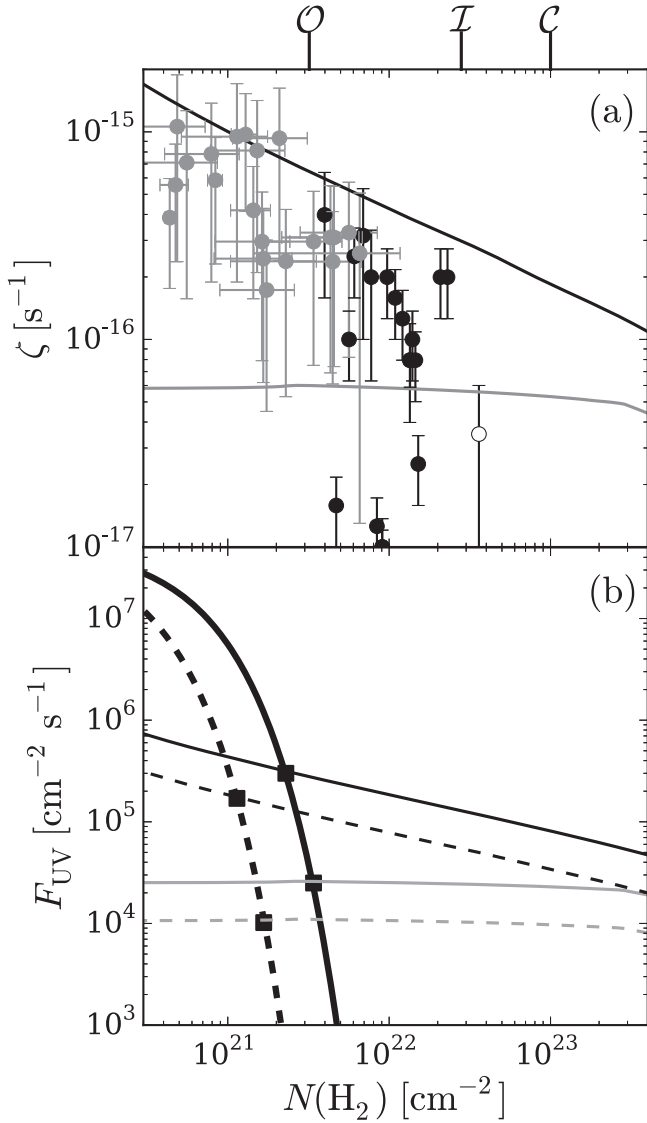


Figure 3. (a) CR ionization rate ζ as a function of the column density of molecular hydrogen $N(\text{H}_2)$ for the model \mathcal{H} (black line) and model \mathcal{L} (gray line), the densities corresponding to the regions \mathcal{O} , \mathcal{I} , and \mathcal{C} are indicated. The symbols are the observational values from Indriolo & McCall (2012, gray solid circles), Caselli et al. (1998, black solid circles), and Maret & Bergin (2007, empty circle). (b) Comparison of the attenuated interstellar flux of UV photons (thick lines) with the local UV flux generated by CRs (thin lines). The thin black and gray lines represent the CR-generated fluxes for the model \mathcal{H} and \mathcal{L} , respectively. The dashed and solid lines show the results for $R_V = 3.1$ and 5.5 , respectively.

Table 2
CR Ionization Rate ζ (s⁻¹) and Plasma Electron Fraction x_e , for Three Characteristic Core Regions (\mathcal{O} , \mathcal{I} , and \mathcal{C}) and Two CR Models (\mathcal{L} and \mathcal{H})

	ζ		x_e	
	Model \mathcal{L}	Model \mathcal{H}	Model \mathcal{L}	Model \mathcal{H}
\mathcal{O}	6.0×10^{-17}	6.5×10^{-16}	9.4×10^{-8}	3.1×10^{-7}
\mathcal{I}	5.6×10^{-17}	3.0×10^{-16}	6.9×10^{-9}	1.6×10^{-8}
\mathcal{C}	5.3×10^{-17}	1.8×10^{-16}	1.3×10^{-9}	2.3×10^{-9}

The relation between the electron and ion densities is determined from the charge neutrality condition,

$$n_e = \sum_i n_i + \langle Z \rangle n_d,$$

where $\langle Z \rangle n_d \equiv \int_{a_{\min}}^{a_{\max}} da \sum_Z Z N_Z(a)$ is the charge number density carried by dust. In starless dense molecular clouds studied in this paper, the dust contribution is negligible as long as the ratio $n(\text{H}_2)/\zeta$ is below a certain value—e.g., for single-size grains of $a = 0.1 \mu\text{m}$, the neutral density should be less than $\sim 10^{11} \text{cm}^{-3}$ (Umebayashi & Nakano 1990), for the MRN distribution (Mathis et al. 1977) the approach works at $n(\text{H}_2) \lesssim 10^7 \text{cm}^{-3}$ (Nakano et al. 2002). Therefore, for the calculations below, we set $n_e = \sum_i n_i$ for all three cloud regions, which implies that our results are independent of details of the grain size distribution and demonstrate the generic CR effects on dust charging.

We note that in situations where the dust contribution to the charge neutrality is not negligible, e.g., at higher $n(\text{H}_2)$, the distribution of grain charges is determined by the particular form of $dn_d(a)/da$ which is quite uncertain inside dense molecular clouds (see, e.g., Kim et al. 1994; Weingartner & Draine 2001a). Some insights into possible forms of the size distribution in such environments can be gained from numerical simulations (see, e.g., Ormel et al. 2009). The role of dust becomes particularly important in dense cores containing protostellar sources, where small grains (the main carriers of negative charge) are abundantly produced due to shock shattering (Guillet et al. 2011).

3.1. “Reference Case”: Cold-plasma Charging

In the usual approach, the dust charging in cold molecular clouds is caused by the collection of electrons and ions from a cold plasma background. The charge distribution in this case is readily obtained by substituting Equations (5) and (6) in Equation (4):

$$\begin{aligned} & \vdots \\ \frac{N_{+1}}{N_0} &= \frac{1}{\sqrt{\tilde{m}}(1 + \tilde{\varphi})}, \\ \frac{N_{-1}}{N_0} &= \frac{\sqrt{\tilde{m}}}{1 + \tilde{\varphi}}, \\ \frac{N_{-2}}{N_{-1}} &= \frac{\sqrt{\tilde{m}} e^{-\tilde{\varphi}}}{1 + 2\tilde{\varphi}}. \\ & \vdots \end{aligned} \quad (7)$$

The distribution depends on two dimensionless numbers: the normalized floating potential of the unit charge (or the inverse normalized temperature) $\tilde{\varphi} = e^2/ak_B T$, and the effective ion-to-electron mass ratio \tilde{m} (or the effective atomic mass number A) determined by the partial contributions of all ions:

$$\tilde{\varphi} \simeq \frac{1.67}{a_\mu T_{10}}, \quad \frac{42.8}{\sqrt{\tilde{m}}} \equiv \frac{1}{\sqrt{A}} \simeq \sum_i \frac{n_i}{n_e} \frac{1}{\sqrt{A_i}},$$

where a_μ is in units of μm , T_{10} is in units of 10 K, and A_i is the atomic mass number of the i th ion species. Both numbers are large: $\tilde{\varphi} \simeq 17$ for $T = 10$ K and the largest grains of the MRN distribution ($a \simeq 0.1 \mu\text{m}$), while $\tilde{m} = 1836$ for a hydrogen plasma. This implies that (1) the abundance of the $Z = -2$ state is exponentially small and (2) one can neglect unity in the denominators of Equation (7), so the ratios $N_{\pm 1}/N_0 \propto aT$ have a simple universal dependence on temperature and dust size. Furthermore, since $N_{-1}/N_{+1} = \tilde{m}$, the negatively charged state

is at least three orders of magnitude more abundant than the positive one.

Thus, submicron grains in a cold plasma are either neutral or singly negatively charged. For a given temperature, most of the dust smaller than $a_\mu \simeq 1.67/(\sqrt{\tilde{m}}T_{10})$ is neutral, while larger grains are mostly negatively charged (for a hydrogen plasma at $T=10$ K, the transition occurs at $a \simeq 400$ Å). This simple scaling holds as long as $\tilde{\varphi} \gg 1$, i.e., for $a_\mu \lesssim T_{10}^{-1}$. Larger grains/aggregates (in the micron-size range, or if the temperature increases) become multiply negatively charged; the charge distribution remains narrow, with the average charge $-\langle Z \rangle$ about a few $\tilde{\varphi}^{-1}$.

3.2. Effect of CRs

Figure 2 demonstrates that the CR proton spectrum at lower energies is by many orders of magnitude lower than the electron spectrum. Therefore, the former gives a negligibly small contribution to the collection flux, as compared to the flux of CR electrons. Following the approach by Draine & Salpeter (1979), we calculate the electron collection flux as

$$J_e^{\text{CR}} \simeq \pi a^2 \int_{E_{\text{int}}}^{\infty} dE 4\pi j_e(E) [s_e(E) - \delta_e(E)], \quad (8)$$

where $s_e(E)$ is the sticking coefficient (probability) for impinging CR electrons and $\delta_e(E)$ is the yield of the secondary electrons (see details in Appendix C). The lower limit of integration is equal to the intersection energy $E_{\text{int}} \simeq 1.5 \times 10^{-2}$ eV, at which the CR electron spectra in Figure 2 cross the Maxwellian curves.

Note that in Equation (8), under the integral we omitted the OML factor $(1 + \varphi_Z/E)$ (see, e.g., Horanyi et al. 1988), which determines the charge dependence of the flux (and leads to Equation (5) for the Maxwellian spectrum). As shown below, the charge distribution is usually concentrated within $|Z| \lesssim 3$; since the magnitude of the floating potential is $e^2/a \sim 10$ meV, while the energy of CR electrons contributing to the charging is $E \sim 10$ eV, the OML correction can be safely neglected and hence J_e^{CR} does not depend on Z .

The photoelectric emission flux from a grain $J^{\text{PE}}(Z)$ is determined by the total specific intensity $I(\nu)$ of the local radiation field, and depends on the photoemission yield $Y(\nu)$ (Weingartner et al. 2006) and the absorption efficiency $Q_{\text{abs}}(\nu)$ (Draine & Hao 2002; Draine 2011). As shown in Figure 3(b), the interstellar UV field (integrated over the frequency range of $10 \text{ eV} \leq h\nu \leq 13.6 \text{ eV}$) is exponentially attenuated with $N(\text{H}_2)$, and so for all three core regions the local radiation is solely due to the H_2 fluorescence generated by CRs. The resulting photoemission flux can be approximately calculated as

$$\begin{aligned} J^{\text{PE}} &= \pi a^2 \int d\nu \frac{4\pi I(\nu)}{h\nu} Y(\nu) Q_{\text{abs}}(\nu) \\ &\simeq \pi a^2 F_{\text{UV}} \langle Y(\nu) Q_{\text{abs}}(\nu) \rangle_{\text{UV}}, \end{aligned}$$

where F_{UV} is given by Equation (3) and $\langle Y(\nu) Q_{\text{abs}}(\nu) \rangle_{\text{UV}}$ is averaged over the Lyman and Werner bands. The latter value may vary for different materials (Weingartner et al. 2006), but this variation is not very significant; for the calculations below, we set $\langle Y(\nu) Q_{\text{abs}}(\nu) \rangle_{\text{UV}} = 0.2$, which corresponds to a carbonaceous grain of $a \sim 0.1 \mu\text{m}$. Here, the dependence of J^{PE} on Z is neglected as well, since photoelectrons have a broad

energy distribution (roughly limited from above by the energy of the UV photons minus the work function, see, e.g., Draine 1978) and, hence, the floating potential cannot noticeably affect the photoemission flux.

Thus, the CR effect on the charge distribution is determined by the collection flux of CR electrons J_e^{CR} and the photoemission flux J^{PE} . These fluxes compete, respectively, with the electron and ion fluxes of a cold plasma background and, hence, their relative magnitude can be conveniently quantified by the dimensionless numbers ϵ_{CR} and ϵ_{PE} :

$$J_e^{\text{CR}} = \epsilon_{\text{CR}} J_e^{\text{M}}(0), \quad J^{\text{PE}} = \epsilon_{\text{PE}} \sum_i J_i^{\text{M}}(0).$$

Both numbers do not depend explicitly on a (a weak implicit dependence on dust size is via $s_e(E,a)$ and $\delta_e(E,a)$ for ϵ_{CR} and via $Y(\nu, a)$ for ϵ_{PE}). From Equations (5) and (6) it follows that $J_e^{\text{M}}(0) \propto n_e \sqrt{T}$ and $\sum_i J_i^{\text{M}}(0) \propto n_e \sqrt{T/A}$, and so the relations to the plasma parameters and the UV flux are given by

$$\epsilon_{\text{CR}} \propto \frac{1}{n_e \sqrt{T}}, \quad \epsilon_{\text{PE}} \propto \frac{F_{\text{UV}}}{n_e} \sqrt{\frac{A}{T}}. \quad (9)$$

The abundances of the singly charged states are straightforwardly derived from Equation (4),

$$\frac{N_{+1}}{N_0} = \frac{1 + \epsilon_{\text{PE}}}{\sqrt{\tilde{m}}(\tilde{\varphi} + \epsilon_{\text{CR}})}, \quad (10)$$

$$\frac{N_{-1}}{N_0} = \frac{\sqrt{\tilde{m}}(1 + \epsilon_{\text{CR}})}{\tilde{\varphi} + \epsilon_{\text{PE}}}, \quad (11)$$

for the multiply charged states the following recurrent relations are obtained:

$$Z \geq 2: \quad \frac{N_{+Z}}{N_{+(Z-1)}} = \frac{\epsilon_{\text{PE}}}{\sqrt{\tilde{m}}(Z\tilde{\varphi} + \epsilon_{\text{CR}})}, \quad (12)$$

$$-Z \geq 2: \quad \frac{N_{-|Z|}}{N_{-(|Z|-1)}} = \frac{\sqrt{\tilde{m}}\epsilon_{\text{CR}}}{|Z|\tilde{\varphi} + \epsilon_{\text{PE}}}. \quad (13)$$

Following the estimates in Section 3.1, the unity was neglected with respect to $\tilde{\varphi}$ in these equations (as one can see by comparing with Equation (7)); for the multiply charged states, we also omitted the exponentially small terms, assuming that $\epsilon_{\text{CR}}, \epsilon_{\text{PE}} \gg e^{-\tilde{\varphi}}$.

The charge distribution is slightly modified when the polarization interactions are taken into account (see, e.g., Equations (3.3) and (3.4) in Draine & Sutin 1987): in Equations (10) and (11), one has to add the term $\sqrt{\pi\tilde{\varphi}}/2$ to the unity in the numerator, and multiply $\tilde{\varphi}$ in the denominator with 2. For the multiply charged states (both positive and negative), one needs to replace $|Z|$ in the denominator of Equations (12) and (13) with the product $\sqrt{|Z|}(\sqrt{|Z|} + 1)$.

One could also take into account the fact that CR electrons (contribution to the collection flux J_e^{CR}) have some finite effective temperature T_{CR} . In this case, the collection flux for $Z < 0$ and, hence, the rhs of Equation (13) has to be multiplied with the OML factor $e^{-|Z|\tilde{\varphi}_{\text{CR}}}$, where $\tilde{\varphi}_{\text{CR}} = e^2/ak_{\text{B}}T_{\text{CR}} = \tilde{\varphi}(T/T_{\text{CR}})$. As we pointed out above, the energy of CR electrons contributing to the charging is of the order of 10 eV, so $\tilde{\varphi}_{\text{CR}}$ is very small ($\lesssim 10^{-2}$ for the parameters used above) and the resulting effect is indeed negligible.

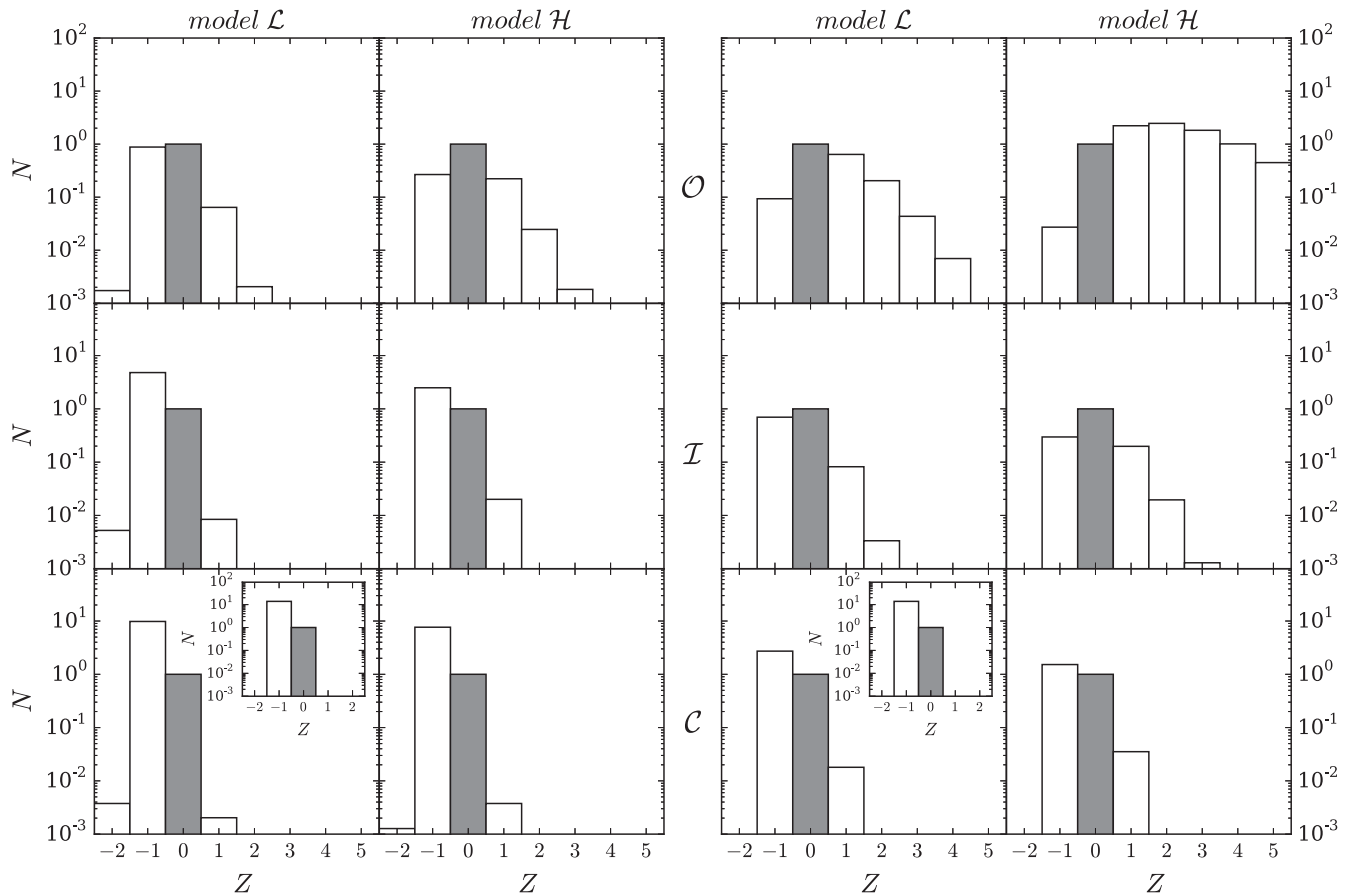


Figure 4. Effect of CRs on the dust charge distribution in dense molecular clouds. The distribution function N_Z is described by Equations (10)–(13), the results for $\bar{\phi} = 17$ and $A = 29$ (HCO^+ ions) are plotted for different CR models (\mathcal{L} and \mathcal{H}) and different characteristic regions (\mathcal{O} , \mathcal{I} , and \mathcal{C}) of the core. The left panel shows the results for typical parameters determining the magnitude of ϵ_{PE} , in the right panel ϵ_{PE} is increased by a factor of 10. The insets in the lower row depict the “reference case,” described by Equation (7), where the CR effects are neglected. The uncharged state $Z = 0$ (shaded) is normalized to unity.

Figure 4 illustrates the CR effect on the charge distribution in different regions of the cloud. The left panel shows N_Z calculated for typical plasma density n_e (from Equation (2)) and parameters determining the magnitude of the CR-generated UV flux F_{UV} (Equation (3) with $\omega = 0.5$ and $R_V = 3.1$). However, both n_e and F_{UV} are known only approximately: the ionization fraction might be a factor of two to three lower than that given by Equation (2) (see, for example, model 1 of Caselli et al. 2002), while the UV flux is approximately doubled for $R_V \gtrsim 5$ (typical for dark dense clouds, see also footnote 7). Furthermore, as pointed out in footnote 6, F_{UV} can exceed the value given by Equation (3) due to the difference between the ionization and excitation cross sections. As one can see from Equation (9), a combination of all of these uncertainly factors may easily increase the value of ϵ_{PE} by an order of magnitude. Therefore, in the right panel we show N_Z for ϵ_{PE} multiplied by 10 (and otherwise the same parameters). The role of CRs in dust charging becomes particularly evident when the obtained results are compared with the “reference” charge distribution depicted in the insets, where the CR effects are neglected.

From Equations (12) and (13) we infer that, generally, the asymptotic form of N_Z at large $|Z|$ is a Poisson distribution $P(Z; \lambda)$: for positive charges, it operates at $Z \gtrsim \epsilon_{\text{CR}}/\bar{\phi}$ and is determined by the Poisson parameter $\lambda_+ = \epsilon_{\text{PE}}/\sqrt{m} \bar{\phi}$ (and, analogously, for negative charges).

Table 3 shows that the collection numbers ϵ_{CR} are *very small* for all considered cases (at least 10^3 times smaller than $\bar{\phi}$). Therefore, from Equations (10) and (12), we conclude that positive charges are not affected by CR collection and have a Poisson distribution for all $Z \geq 2$; the corresponding Poisson parameter in the region \mathcal{O} can be as large as $\lambda_+ \simeq 0.4$ and $\simeq 3.1$ for the models \mathcal{L} and \mathcal{H} , respectively (right panel of Figure 4; for the regions \mathcal{I} and \mathcal{C} , $\lambda_+ \ll 1$). On the contrary, the photoemission numbers ϵ_{PE} are usually *large* ($\epsilon_{\text{PE}} \gg \bar{\phi}$, except for the densest \mathcal{C} case) and the distribution of negative charges is completely dominated by the state $Z = -1$, whose abundance is given by Equation (11); for $|Z| \geq 2$, it abruptly decreases as $N_Z \propto (\sqrt{m} \epsilon_{\text{CR}}/\epsilon_{\text{PE}})^{|Z|}$, with $\sqrt{m} \epsilon_{\text{CR}}/\epsilon_{\text{PE}} \lesssim 3 \times 10^{-3}$.

We conclude that in all regions of the cloud, the equilibrium charge distribution is governed by a competition between the cold-plasma collection (providing negative charging) and the photoemission due to the CR-generated UV field (which leads to positive charging). The effect of photoemission is dominant in the region \mathcal{O} , quite significant in the region \mathcal{I} (particularly, in the right panel of Figure 4), and still noticeable in the densest region \mathcal{C} . The direct effect of CRs on dust charging—the collection of suprathermal CR electrons—is negligible for all considered situations.

3.3. Dependence on the Ion Mass and Grain Size

The results, shown in Figure 4 for HCO^+ ions, remain practically unchanged for other ions also: from Equation (9) it

Table 3
Dimensionless Numbers ϵ_{CR} and ϵ_{PE} Characterizing the CR Effect

	ϵ_{CR}		ϵ_{PE}	
	Model \mathcal{L}	Model \mathcal{H}	Model \mathcal{L}	Model \mathcal{H}
\mathcal{O}	2.67×10^{-3}	9.33×10^{-3}	2.38×10^2	8.71×10^2
\mathcal{I}	3.35×10^{-4}	1.34×10^{-4}	29.7	74.3
\mathcal{C}	8.56×10^{-5}	4.31×10^{-5}	7.55	15.0

Note. The values correspond to conditions for the left panel of Figure 4. For the right panel, ϵ_{PE} should be multiplied by 10; for different ions it should be rescaled as $\epsilon_{\text{PE}} \propto \sqrt{A}$.

follows that $\epsilon_{\text{PE}} \propto \sqrt{\tilde{m}}$, and therefore the charge distribution for $Z > 0$ (Equations (10) and (12)) does not depend on \tilde{m} as long as $\epsilon_{\text{PE}} \gg 1$, i.e., for all considered cases. For $Z < 0$ (Equations (11) and (13)), the distribution is unchanged when $\epsilon_{\text{PE}} \gg \tilde{\varphi}$. From Table 3, we see that this condition is only violated in the densest region \mathcal{C} with the “typical” parameters (left panel of Figure 4), where $N_{-1}/N_0 \propto \sqrt{\tilde{m}}$.

Using the same consideration, one can also obtain the dependence of N_Z on the grain size: from Equations (10) and (12), we see that, as long as $\tilde{\varphi} \gg 1$, the relative abundance of the positively charged states varies as $N_Z/N_0 \propto \tilde{\varphi}^{-1} \propto a$. Similar to the dependence on \tilde{m} , the distribution of negative charges depends on a only in the region \mathcal{C} , where $\epsilon_{\text{PE}} \lesssim \tilde{\varphi}$; in the regions \mathcal{O} and \mathcal{I} , the size dependence sets in when the term $e^{-\tilde{\varphi}}$, neglected in Equation (13) (see last Equation (7)), becomes comparable to ϵ_{CR} . The latter occurs for sizes $a_\mu \geq 1.7/(T_{10} \ln \epsilon_{\text{CR}}^{-1})$ which are larger than the upper cutoff a_{max} of the MRN distribution.

By employing these simple scaling relations and using the examples presented in Figure 4, one can easily deduce the form of N_Z for arbitrary plasma composition and grain size.

3.4. Implications

Knowing the charge distribution on dust grains in dense molecular clouds is important for several reasons: the charges modify the cross sections of the ion accretion on dust, thus critically changing the surface chemistry, influencing the formation of grain mantles, etc. For the same reason, the charges change the total energy balance of grains and, hence, may alter the equilibrium temperature. However, the most profound effect can be on the rate of dust coagulation (Dominik et al. 2007, p.783). Let us briefly elaborate on this important point.

Using the derived charge distributions, one can identify the “optimum” balance between the positive and negative charges, for which the rate of dust coagulation is maximized. Conditions for such a balance is particularly easy to obtain when the distribution of positive charges monotonously decreases with Z (i.e., when $\lambda_+ < 1$). The coagulation rate in this case is maximized when $N_{+1} \sim N_{-1}$. For $\epsilon_{\text{CR}} \ll 1$ and $1 \ll \tilde{\varphi} \ll \epsilon_{\text{PE}}$ (see Table 3), from Equations (10) and (11), we obtain the “optimum” relation: $\epsilon_{\text{PE}}^{\text{opt}} \sim \sqrt{\tilde{m}\tilde{\varphi}}$.

Remarkably, the optimum relation becomes size-independent at late stages of dust coagulation: when the resulting clusters grow well beyond the upper cutoff size of the MRN distribution, so that $\tilde{\varphi} \lesssim 1$, one has to replace $\tilde{\varphi}$ with unity (neglected in Equations (10) and (11)). This yields

$$\epsilon_{\text{PE}}^{\text{opt}}/\sqrt{\tilde{m}} \sim 1.$$

Furthermore, since $\epsilon_{\text{PE}} \propto \sqrt{\tilde{m}}$, the coagulation optimum does not depend on the plasma composition either and, hence, is universal. As one can see from Table 3, the optimum is attained somewhere between the regions \mathcal{O} and \mathcal{I} , which corresponds to the densities $n(\text{H}_2)$ between $\sim 10^4$ and $\sim 10^6 \text{ cm}^{-3}$.

The existence of the coagulation optimum is in striking contrast with the case of pure plasma charging, where growing negative charges on clusters inhibit their further coagulation (Okuzumi 2009). Thus, CRs can provide ideal conditions for a rapid dust coagulation in cold dense molecular clouds. We will discuss this important effect in a separate paper.

4. CONCLUSIONS

The aim of this paper is to demonstrate that CRs strongly affect charging of dust grains in cold dense molecular clouds.

We calculated the local (propagated) CR spectra for three characteristic regions of a dense core and investigated the two mechanisms of dust charging that have been ignored so far: collection of suprathermal CR electrons and protons by grains (adding to the cold Maxwellian plasma collection), and photoelectric emission from grains due to the CR-generated UV field. While the former mechanism turns out to always be negligible, the photoemission is shown to dramatically modify the charge distribution for submicron grains in almost the entire cloud (as compared to the “reference case” of cold-plasma charging). The competition between the cold-plasma collection (producing, primarily, singly charged negative grains) and the photoemission (resulting in positive charging) significantly broadens the charge distribution.

The relative magnitude of the CR-induced photoemission is quantified by the dimensionless number ϵ_{PE} . This number depends on several physical parameters, some of them being only approximately known. The main sources of uncertainty are the values of the ionization fraction x_e and the CR-induced UV flux F_{UV} : as we pointed out in Section 3.2, the uncertainty in x_e is mainly due to competition between different recombination processes, while F_{UV} , in turn, is determined by (approximately known) dust albedo, extinction slope, and photoemission yield, as well as by (partially unknown) H_2 excitation rates. To take all of these factors into account, in Figure 4, we presented two sets of plots showing the dust charge distribution: the left and right panels correspond to the expected “typical” and “maximum” values of ϵ_{PE} and, thus, demonstrate the extent to which the integral effect of uncertainties may affect the final results.

Our results have several important implications. The shown modification of the grain charge distribution considerably changes the rates of ion accretion on dust, which in turn can critically change the surface chemistry, alter the total energy balance of grains, influence the formation of icy mantles, etc. These CR effects are particularly strong in the outer regions of the core, where the charge distribution is dominated by positive grains and, hence, the accretion of negatively charged ions should be drastically reduced.

The most profound effect of CRs is expected to occur for the rate of dust coagulation: when the cold-plasma collection is the only charging mechanism operating in a cloud, the average (negative) dust charge increases proportionally to the size. Therefore, the growing Coulomb repulsion inhibits coagulation of larger ($\gtrsim 1 \mu\text{m}$) aggregates. Here we showed that the competition between the cold-plasma collection and photoemission can create approximately equal abundance of

positively and negatively charged dust, providing “optimum” conditions for coagulations. The derived optimum is size-independent for large dust, which enables the growth of big aggregates.

The presented results are obtained assuming that charged dust does not affect the overall charge neutrality in a cloud. Although this assumption can be violated for sufficiently dense regions, our approach can be straightforwardly extended to this case as well, provided the dust size distribution is known. Furthermore, the described effects of CRs are of a generic nature, and are expected to operate not only in dense molecular clouds but also in the upper layers and the outer parts of protoplanetary disks, where mutual sticking of dust aggregates is the essential process toward planetesimal formation.

The authors thank the referee, A. Jones, for providing helpful and constructive comments and suggestions. The authors also acknowledge Malcolm Walmsley for a critical reading of the manuscript and helpful comments. M.P. acknowledges the support of the OCEVU Labex (ANR-11-LABX-0060) and the A*MIDEX project (ANR-11-IDEX-0001-02) funded by the “Investissements d’Avenir” French government program managed by the ANR. M.P. and D.G. acknowledge the support of the CNRS-INAF PICS project “Pulsar wind nebulae, supernova remnants and the origin of cosmic rays.” P.C. acknowledges support from the European Research Council (ERC, project PALs 320620).

APPENDIX A COULOMB LOSS FUNCTIONS

In order to combine the propagated CR spectra obtained in Padovani et al. (2009) with the cold Maxwellian plasma background, the energy loss functions $L_k(E)$ (plotted in Figure 7 of Padovani et al. 2009) have to be extended to lower energies (down to about 1 meV), to include Coulomb losses that dominate in this energy range. The Coulomb loss term, $L_k^C(E)$, is parameterized for protons by Schlickeiser (2002) as

$$L_p^C(E) \simeq 4.8 \times 10^{-10} x_e E^{-1} \text{ eV cm}^2,$$

where x_e is the ionization fraction, the proton energy E (in eV) is supposed to exceed $\sim 3k_B T$. For Coulomb electron losses, we used the analytic fit by Swartz et al. (1971),

$$L_e^C(E) \simeq 5.7 x_e E^{-0.94} \text{ eV cm}^2.$$

Dense cores have typical temperatures of about 10 K, so $k_B T \simeq 9 \times 10^{-4} \text{ eV}$. Figure 5 shows the energy loss functions from Padovani et al. (2009) with the Coulomb terms included, assuming an average ionization fraction of $x_e = 10^{-7}$.

APPENDIX B SPECIFIC INTENSITY OF SECONDARY ELECTRONS

After crossing a column density $dN = n dx$ in medium of density n , an electron of energy E , and velocity v_e has lost an energy $dE = -L_e(E) dN$, where $L_e(E)$ is the energy loss function of electrons,

$$L_e(E) = -\frac{1}{n} \frac{dE}{dx} = -\frac{1}{n v_e} \frac{dE}{dt}, \quad (14)$$

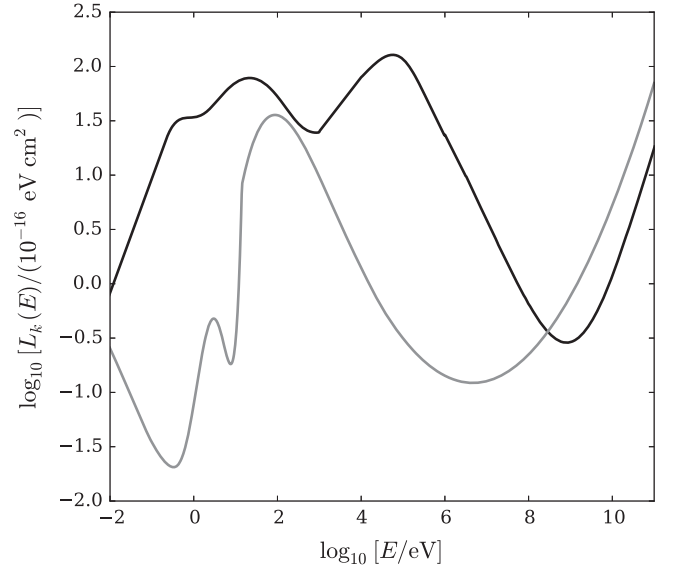


Figure 5. Energy loss functions for protons (black) and electrons (gray). The ionization fraction $x_e = 10^{-7}$ has been assumed to include Coulomb losses.

(and similarly for protons). The column density N_{stop} required to stop an electron of the initial energy E ,

$$N_{\text{stop}}(E) = \int_0^E \frac{dE'}{L_e(E')},$$

has a constant value $N_{\text{stop}}(E) \sim 10^{18} \text{ cm}^{-2}$ up to $E \sim 1 \text{ keV}$ (see Figure 8 in Padovani et al. 2009), and then increases weakly with energy. This short range of secondary electrons, in comparison with typical column densities of molecular clouds ($\sim 10^{22} - 10^{23} \text{ cm}^{-2}$) justifies a local treatment of ionization. In this “on-the-spot” approximation, the stopping time of secondary electrons is

$$\tau_{\text{stop}}(E) \simeq \frac{E}{n v_e L_e(E)}, \quad (15)$$

and their stopping range is $\sim v_e \tau_{\text{stop}} \simeq E/[n L_e(E)]$.

Assuming isotropy, the number of first-generation secondary electrons of energy E (per unit energy, volume and time) is calculated as

$$\frac{dN_e^{\text{sec}}}{dE dV dt} = 4\pi n \int_{I+E}^{\infty} dE' j_k(E') \frac{d\sigma_k^{\text{ion}}}{dE}(E, E'),$$

where $I = 15.6 \text{ eV}$ is the ionization potential of H_2 , $j_k(E')$ is the intensity of primary species k , and $d\sigma_k^{\text{ion}}/dE$ is the corresponding differential ionization cross section. The number of secondary electrons produced per unit energy and volume is then

$$\begin{aligned} \frac{dN_e^{\text{sec}}}{dE dV} &\simeq \frac{dN_e^{\text{sec}}}{dE dV dt} \tau_{\text{stop}} \\ &= \frac{4\pi E}{v_e L_e(E)} \int_{I+E}^{\infty} dE' j_k(E') \frac{d\sigma_k^{\text{ion}}}{dE}(E, E'). \end{aligned}$$

This quantity is related to the specific intensity of secondary electrons $j_e^{\text{sec}}(E)$ (number of electrons per unit energy, area,

time, and solid angle) by $dN_e^{\text{sec}}/dE dV = (4\pi/v_e)j_e^{\text{sec}}$, which finally yields

$$j_e^{\text{sec}}(E) \simeq \frac{E}{L_e(E)} \int_{I+E}^{\infty} dE' j_k(E') \frac{d\sigma_k^{\text{ion}}}{dE}(E, E'). \quad (16)$$

Equation (16) is iterated, to compute intensities for the next generations of secondary electrons.

APPENDIX C ELECTRON STICKING PROBABILITY AND SECONDARY EMISSION YIELD

Following Draine & Salpeter (1979), we set the sticking probability $s_e(E)$ equal to unity if the electron stopping range $R_e(E)$ (in the dust material) is smaller than $4a/3$, otherwise $s_e(E) = 0$. The transition energy varies with dust size as $\propto a^{2/3}$; for sub-micron grains, $a \sim 0.1 \mu\text{m}$, the transition occurs at $E \sim 3 \text{ keV}$. The electron trapping by small (polycyclic aromatic hydrocarbon) grains was calculated by Micelotta et al. (2010).

The secondary emission yield $\delta_e(E)$ is obtained by averaging over the velocity distributions of the emitted electrons, which are believed to be broad (non-Maxwellian), decaying as E^{-1} at large energies (Draine & Salpeter 1979). For a positively charged dust, the explicit dependence on φ_Z is approximated by $\delta_e \propto 1/\sqrt{1 + (\varphi_Z/E_*)^2}$, where $E_* \sim 3 \text{ eV}$. This factor can be neglected using the same reasoning as for the OML correction factor omitted in Equation (8). For the dependence on E , we employ the Sternglass formula (Horanyi et al. 1988),

$$\frac{\delta_e(E)}{\delta_e^{\text{max}}} = \frac{E}{E_{\text{max}}} \exp\left(2 - 2\sqrt{\frac{E}{E_{\text{max}}}}\right),$$

where the value of δ_e^{max} is typically between 1.5 and 2.5, and $E_{\text{max}} = 0.2\text{--}0.4 \text{ keV}$ (Draine & Salpeter 1979). Note that $\delta_e(E)$ has a finite-size correction at large E , which increases the yield by a factor of $\simeq 1.6$.

REFERENCES

- Aguilar, M., Aisa, D., Alpat, B., et al. 2015, *PhRvL*, **114**, 171103
Aguilar, M., Aisa, D., Alvino, A., et al. 2014, *PhRvL*, **113**, 121102
Alves, J. F., Lada, C. J., & Lada, E. A. 2001, *Natur*, **409**, 159
André, P., Di Francesco, J., Ward-Thompson, D., et al. 2014, in *Protostars and Planets VI*, ed. H. Beuther et al. (Tucson, AZ: Univ. of Arizona Press), 27
Bakes, E. L. O., & Tielens, A. G. G. M. 1994, *ApJ*, **427**, 822
Blumenthal, G. R., & Gould, R. J. 1970, *RvMP*, **42**, 237
Bonnor, W. B. 1956, *MNRAS*, **116**, 351
Burlaga, L. F., & Ness, N. F. 2014, *ApJL*, **795**, L19
Caselli, P., Walmsley, C. M., Terzieva, R., & Herbst, E. 1998, *ApJ*, **499**, 234
Caselli, P., Walmsley, C. M., Zucconi, A., et al. 2002, *ApJ*, **565**, 344
Cecchi-Pestellini, C., & Aiello, S. 1992, *MNRAS*, **258**, 125
Dominik, C., Blum, J., Cuzzi, J. N., & Wurm, G. 2007, in *Protostars and Planets V*, ed. B. Reipurth, D. Jewitt & K. Keli (Tucson, AZ: Univ. of Arizona Press), 783
Draine, B. T. 1978, *ApJS*, **36**, 595
Draine, B. T. 2011, *Physics of the Interstellar and Intergalactic Medium* (Princeton, NJ: Princeton Univ. Press)
Draine, B. T., & Hao, L. 2002, *ApJ*, **569**, 780
Draine, B. T., & Salpeter, E. E. 1979, *ApJ*, **231**, 77
Draine, B. T., & Sutin, B. 1987, *ApJ*, **320**, 803
Ebert, R. 1955, *ZAp*, **37**, 217
Elmegreen, B. G. 1979, *ApJ*, **232**, 729
Fortov, V. E., Ivlev, A. V., Khrapak, S. A., Khrapak, A. G., & Morfill, G. E. 2005, *PhR*, **421**, 1
Gordon, K. D. 2004, in *ASP Conf. Ser. 309, Astrophysics of Dust*, ed. A. N. Witt, G. C. Clayton & B. T. Draine (San Francisco, CA: ASP), 77
Guillet, V., Pineau Des Forêts, G., & Jones, A. P. 2011, *A&A*, **527**, A123
Horanyi, M., Houppis, H. L. F., & Mendis, D. A. 1988, *Ap&SS*, **144**, 215
Indriolo, N., & McCall, B. J. 2012, *ApJ*, **745**, 91
Kamae, T., Karlsson, N., Mizuno, T., Abe, T., & Koi, T. 2006, *ApJ*, **647**, 692
Keto, E., & Caselli, P. 2008, *ApJ*, **683**, 238
Keto, E., & Caselli, P. 2010, *MNRAS*, **402**, 1625
Kim, S.-H., Martin, P. G., & Hendry, P. D. 1994, *ApJ*, **422**, 164
Maret, S., & Bergin, E. A. 2007, *ApJ*, **664**, 956
Mathis, J. S., Rumpl, W., & Nordsieck, K. H. 1977, *ApJ*, **217**, 425
McKee, C. F. 1989, *ApJ*, **345**, 782
Mestel, L., & Spitzer, L., Jr. 1956, *MNRAS*, **116**, 503
Micelotta, E. R., Jones, A. P., & Tielens, A. G. G. M. 2010, *A&A*, **510**, A37
Morlino, G., & Gabici, S. 2015, *MNRAS*, **451**, L100
Nakano, T., Nishi, R., & Umebayashi, T. 2002, *ApJ*, **573**, 199
Nishi, R., Nakano, T., & Umebayashi, T. 1991, *ApJ*, **368**, 181
Okuzumi, S. 2009, *ApJ*, **698**, 1122
Oppenheimer, M., & Dalgarno, A. 1974, *ApJ*, **192**, 29
Ormel, C. W., Paszun, D., Dominik, C., & Tielens, A. G. G. M. 2009, *A&A*, **502**, 845
Padovani, M., & Galli, D. 2011, *A&A*, **530**, A109
Padovani, M., Galli, D., & Glassgold, A. E. 2009, *A&A*, **501**, 619
Padovani, M., Galli, D., Hennebelle, P., Commerçon, B., & Joos, M. 2014, *A&A*, **571**, A33
Padovani, M., Hennebelle, P., & Galli, D. 2013, *A&A*, **560**, A114
Putze, A., Maurin, D., & Donato, F. 2011, *A&A*, **526**, A101
Roman-Duval, J., Jackson, J. M., Heyer, M., Rathborne, J., & Simon, R. 2010, *ApJ*, **723**, 492
Scherer, K., Fichtner, H., Ferreira, S. E. S., Büsching, I., & Potgieter, M. S. 2008, *ApJL*, **680**, L105
Schlickeiser, R. 2002, *Cosmic Ray Astrophysics* (Berlin: Springer)
Shchekinov, Yu. A. 2007, *A&AT*, **26**, 227
Shu, F. H., Galli, D., Lizano, S., & Cai, M. 2006, *ApJ*, **647**, 382
Spitzer, L., Jr. 1941, *ApJ*, **93**, 369
Stone, E. C., Cummings, A. C., McDonald, F. B., et al. 2013, *Sci*, **341**, 150
Swartz, W. E., Nisbet, J. S., & Green, A. E. S. 1971, *JGR*, **76**, 8425
Tafalla, M., Myers, P. C., Caselli, P., Walmsley, C. M., & Comito, C. 2002, *ApJ*, **569**, 815
Umebayashi, T., & Nakano, T. 1980, *PASJ*, **32**, 405
Umebayashi, T., & Nakano, T. 1990, *MNRAS*, **243**, 103
Wardle, M., & Ng, C. 1999, *MNRAS*, **303**, 239
Watson, W. D. 1974, *ApJ*, **188**, 35
Webber, W. R. 1998, *ApJ*, **506**, 329
Weingartner, J. C., & Draine, B. T. 2001a, *ApJ*, **548**, 296
Weingartner, J. C., & Draine, B. T. 2001b, *ApJS*, **134**, 263
Weingartner, J. C., Draine, B. T., & Barr, D. K. 2006, *ApJ*, **645**, 1188
Whipple, E. C. 1981, *RPPH*, **44**, 1197